RSC Advances

ROYAL SOCIETY OF CHEMISTRY

www.rsc.org/advances

RSC Advances

ARTICLE

Green synthesis of bifunctional Fe-montmorillonite composite during Fenton degradation process and its enhanced adsorption and heterogeneous photo-Fenton catalytic properties

Received 00th January 20xx,
Accepted 00th January 20xx

DOI: 10.1039/x0xx00000x

www.rsc.org/

Sheng Guo and Gaoke Zhang*

A novel Fe-MMT-I composite was synthesized during the degradation of rhodamine B (RhB) through Fenton's method, which could degrade RhB (concentration as high as 1000 mg/L), reuse iron sludge and obtain high efficient bifunctional composite at the same time. X-ray diffraction analysis confirmed the existence of FeOOH in the composite. It is interesting to observe that the introduction of RhB leads more FeOOH inserted into the layer of MMT, which enhanced both adsorption and heterogeneous photo-Fenton activities of the composite. The Fe-MMT-I was efficient for the adsorption of RhB over a wide pH range (2.06-9.72). The Fe-MMT-RhB still exhibited high adsorption capacity toward RhB even after five recycles using heterogeneous Fenton method to regenerate the spent adsorbent. Furthermore, the Fe-MMT-I composite showed high efficiency for photo-Fenton discoloration of RhB with wide operating pH range (2.01-11.67). Photoluminescence measurement and leaching test demonstrated that the discoloration of RhB by the composite could be attributed to the synergetic effects of the enhanced adsorption power of the composite and the hydroxyl radicals initiated through heterogeneous photo-Fenton process. The green method could lead to the construction of combined homogeneous and heterogeneous Fenton processes, which gives new insight into fabricating novel bifunctional composites for environmental remediation.

1. Introduction

In recent years, Fenton process has been proved as one of the most promising advanced oxidation processes, which is widely used for wastewater treatment due to its unique advantages such as low cost, nonselective reactivity, high degradation efficiency and green process [1, 2]. On the other hand, the classic Fenton process exhibits extremely low efficiency at pH>4 and the removal of iron sludge after reaction requires a complex and expensive process, which makes the process non-economical [3]. Thus, the development of heterogeneous Fenton process which can eliminate pollutants in a wide pH range with less iron leaching has attracted more and more attention [4, 5].

Montmorillonite (MMT) encompasses a structural unit-layer consisting of an octahedral layer intercalated between two tetrahedral layers, which are primarily composed of $(Al_4(OH)_{12})$ and SiO_4 entities, respectively. The high specific surface area, chemical stability and excellent cation exchange capacity have opened the way to various applications of MMT as adsorbent, drug carrier and heterogeneous catalyst support [6-8]. Polubesova et al [9] prepared Fe(III)-MMT by impregnation method and used it for the adsorption and oxidative transformation of phenolic acids. Peng et al [10] fabricated Cu/Fe-MMT composite using NaOH as the pillaring agent, the composite showed high adsorption capacity toward humic acid. Daud et al [11] prepared Fe-MMT composite using the impregnation method followed calcination, the composite was efficient for the heterogeneous Fenton discoloration of Acid red 1. However, to the best of our knowledge, no report uses the iron sludge generated from Fenton process as the iron source for the preparation of Fe-MMT composite.

Based on this new idea, we reported a novel way of synthesizing the bifunctional Fe-loaded MMT (Fe-MMT-I) composite during the Fenton degradation of rhodamine B (RhB) for the first time. This method could eliminate RhB (concentration as high as 1000 mg/L), reuse iron sludge and obtain high efficient bifunctional composite at the same time. The as-prepared composite was used as both adsorbent and heterogeneous photo-Fenton catalyst for the removal of RhB. The adsorption kinetic and isotherm models as well as the heterogeneous photo-Fenton activity of the composite were investigated in detail. Moreover, the regeneration of the spent adsorbent was studied by a heterogeneous photo-Fenton process. The green method could lead to the construction of combined homogeneous and heterogeneous Fenton processes, which gives new insight into fabricating novel bifunctional composites for environmental remediation.

2. Experimental

School of Resources and Environmental Engineering, Wuhan University of Technology, Wuhan, 430070, P.R.China. E-mail: gkzhang@whut.edu.cn
Tel: 86-27-87651816; fax: 86-27-87887445.

2.1 Materials

The MMT used in this study came from Anji, Zhejiang, P. R. China. The main components of the Anji montmorillonite are SiO_2 (68.25%), Al_2O_3 (13.37%), Fe_2O_3 (1.56%), Na_2O (3.74%), MgO (3.22%), CaO (1.20%), and K_2O (0.12%). All chemicals were analytical grade reagents and were used as received without further purification. Deionized water was used in all experiments.

2.2 Synthesis of Fe-MMT-I composite

The Fe-MMT-I composite was prepared during the Fenton degradation of RhB. Typically, 2 g of the MMT was dispersed in 200 mL of RhB solution (1000 mg/L) under vigorous agitation for 20 min. After 1.39 g of $FeSO_4 \cdot 7H_2O$ was added to the solution and stirred for another 20 min, 10 mL H_2O_2 (30 wt %) was added dropwise into the above mixture under vigorous stirring for 1 h. The precipitate was collected by centrifuging, washed with deionized water several times and then dried in air at 105 °C. The Fe-MMT was prepared under the same conditions without adding RhB. The FeOOH was fabricated without adding the MMT and RhB. The Fe-MMT-II was synthesized under the same conditions except changing RhB into acid red G (ARG). The schematic diagram for the preparation processes is presented in Fig. 1.

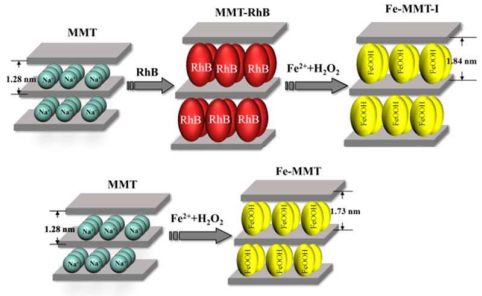

Fig. 1 Schematic diagram for the preparation processes of Fe-MMT and Fe-MMT-I.

2.3 Characterization

X-ray power diffraction (XRD) patterns were obtained on a D/MAX-RB diffractometer with Cu Kα radiation. The morphologies were detected on a JSM-5610LV scanning electron microscopy (SEM) (JEOL, Japan). The chemical bonds on the surface of samples were analyzed by a Nexus Fourier transform infrared (FT-IR) spectroscopy (Thermo Nicolet). Thermogravimetry (TG) analysis of the samples was carried out using a Netzsch STA 449C Jupiter Aeolos (German) coupled to mass spectrometer with a heating rate of 10 °C/min in air. The Brunauer-Emmett-Teller (BET) surface areas of the samples were measured through N_2 adsorption-desorption isotherms using an Autosorb-1 nitrogen adsorption apparatus (Micromeritics, USA).

2.4 Adsorption and degradation experiments

Batch adsorption experiments were carried out in a flask with 30 mg of samples and 100 mL RhB solution with different concentrations of 50-160 mg/L at pH 4.0. The flasks were shaken on a shaker for 12 h with a speed of 160 rpm. The kinetic studies were carried out with 50 mg/L initial concentration of RhB solutions at 25, 35 and 45 °C. The solution pH values were adjusted with dilute HCl or NaOH solution using a pH meter (Mettler Toledo Group, Delta 320).

The degradation experiments were performed in a photo-reactor using a 300 W Dy lamp with a 400 nm cutoff filter. Typically, 50 mg of the sample was dispersed into 100 mL of RhB solution (100 mg/L) aqueous solution. The degradation was initiated by adding 1 mL of the H_2O_2 solution (3%) under magnetic stirring and visible light (vis) irradiation. For desorption and recycle studies, the RhB saturated Fe-MMT-I was added into 100 mL of deionized water. After 1 mL of the H_2O_2 solution (3%) was added, the solution was maintained under vis irradiation for 2 h. Then the spent sample was separated, dried and used in the next run.

At given reaction time intervals, a small volume of the solution was sampled, centrifuged and determined using a UV-vis spectrophotometer (UV1750, Japan). The photoluminescence (PL) spectra were detected by a RF-5301PC spectrophotometer (Shimadzu Corporation, Japan). The total iron leaching was monitored according to the 1, 10-phenanthroline method [12].

3. Results and discussion

3.1 XRD analysis

Fig. 2 shows the XRD patterns of the original MMT, Fe-MMT and Fe-MMT-I. The (001) diffraction peak of MMT appears at 2θ=6.90°, with basal spacing of 1.28 nm. Other characteristic peaks are shown at 2θ of 19.86°, 36.20° and 62.08°, corresponding to the d(020), d(110) and d(060) planes of MMT, respectively [13]. The peaks at 21.86° and 28.90° represent the presence of quartz in the sample. After Fenton oxidization, the d(001) reflection for basal spacing shifted from 1.28 nm (MMT) to 1.73 nm (Fe-MMT). This proves the successful insertion of hydroxyl ferric into the interspaces of MMT. Moreover, it is noticed that a new peak appeared at 35.10°, which could be assigned to the formation of FeOOH [14]. It is interesting to find that the basal spacing of the Fe-MMT-I (1.84 nm) was further increased as compared to that of the Fe-MMT (1.73 nm). The reason could be that when RhB was introduced to the Fenton system, it was firstly absorbed into the layer of MMT due to ion-exchange. During the Fenton degradation process, more hydroxyl ferric was inserted into the layer hence increased the basal spacing of MMT.

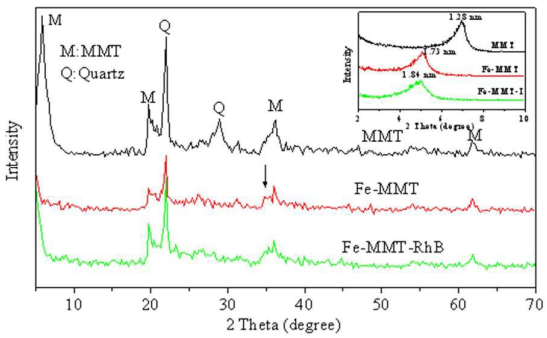

Fig. 2 XRD patterns of MMT, Fe-MMT and Fe-MMT-I.

3.2 SEM images

The morphology and microstructure of the original MMT, Fe-MMT and Fe-MMT-I were investigated by SEM. As shown in Fig. 3a and b, the original MMT is observed as massive and aggregated irregular flakes with particle size of 5-30 µm. After Fenton process, the aggregates were foliated with smoother surfaces with non-uniform particle distribution of 10-50 µm. Many small aggregates of platy particles with irregular shape on the surface were detected (Fig. 3c and d). This is because hydroxyl ferric was mainly impregnated on the surface of the sample. The surface of the Fe-MMT-I was coarser than that of the Fe-MMT (Fig. 3e and f), which could be result from the fact that most of hydroxyl ferric was incorporated into the framework of MMT. The result is in good agreement with the XRD analysis.

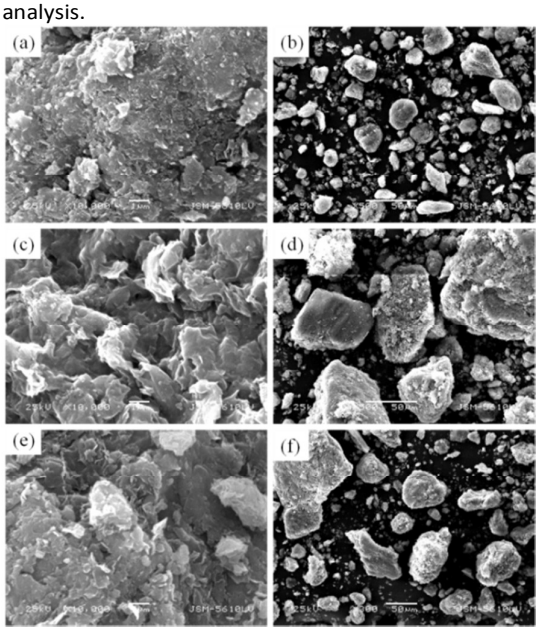

Fig. 3 SEM images of MMT, Fe-MMT and Fe-MMT-I.

3.3 FT-IR analysis

FT-IR spectroscopy was used to gain insights into the chemical bonds on the surface of the original MMT, Fe-MMT and Fe-MMT-I. As shown in Fig. 4, the spectrum of the MMT shows characteristic band at 3620 cm^{-1}, which corresponds to –OH band stretch for Al–OH. The absorption peaks at 3442 and 1636 cm^{-1} could be assigned to –OH stretching band and H–O–H bending mode of the absorbed water. The characteristic peaks at 1090, 1036 and 796 cm^{-1} are attributed to the out-of plane Si–O stretching, in-plane Si–O stretching vibration and Si–O in SiO_2, respectively. The peaks at 915, 846, 623, 519 and 468 cm^{-1} are due to Al–Al–OH, Al–Mg–OH, Si–O, Al–O–Si and Si–O–Fe bending vibrations, respectively [15, 16]. In contrast with MMT, the spectrum of Fe-MMT does not show significant change except the disappearance of a small peak at 1758 cm^{-1}, this is because of the interference of the background of MMT. The result also indicates that the structure of MMT was not destroyed during the Fenton oxidation process. Compared with the spectrum of Fe-MMT, no additional peak can be observed from the spectrum of Fe-MMT-I, indicating that RhB was degraded completely during the preparation process.

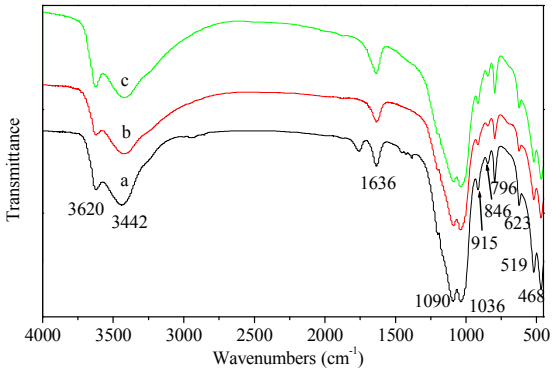

Fig. 4 FT-IR spectra of (a) MMT, (b) Fe-MMT and (c) Fe-MMT-I.

3.4 TG analysis

Fig. 5 presents the TG curves of the original MMT, Fe-MMT and Fe-MMT-I. For MMT, the first weight loss occurs below 150 °C corresponds to the removal of physically adsorbed water. A very small weight loss appears between 150 and 500 °C could be assigned to the removal of interlayer water and the onset of dehydroxilation. The finally weight loss observed between 500 and 800 °C with an inflection point around 700 °C could be attributed to the collapse of the MMT structure [17, 18]. The weight loss of the Fe-MMT and Fe-MMT-I are greater than that of the MMT, nevertheless, the trends are nearly the same. It is interesting to notice that the thermal stability of Fe-MMT-I is higher than that of the Fe-MMT. This confirms that the presence of RhB leads to the insertion of hydroxyl ferric into the layers of MMT which makes the composite more stable. The result is in accordance with those of the XRD and SEM analyses.

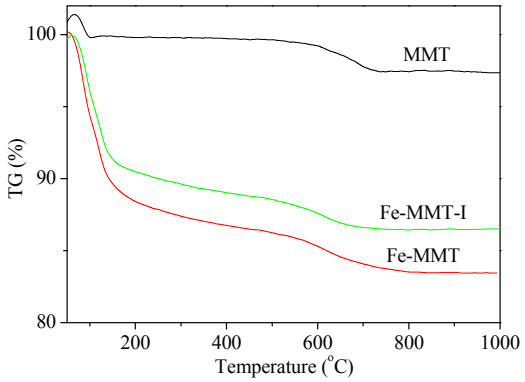

Fig. 5 TG curves of the original MMT, Fe-MMT and Fe-MMT-I.

3.5 Nitrogen adsorption-desorption isotherms

Fig. 6 illustrates the N_2 adsorption-desorption isotherms and pore size distribution curves of the original MMT, Fe-MMT and Fe-MMT-I. According to the IUPAC classification, all these samples exhibit nearly IV type isotherms with hysteresis loops of H3 type, which are the characteristic of the mesoporous materials with slit-shaped pores that are closely related to the layer structure of MMT [19]. The results of the textural properties of the samples are summarized in Table 1. It can be seen that the BET surface area of the original MMT is higher

than those of the Fe-MMT and the Fe-MMT-I. The reason could be that after Fenton oxidation, though the layered structure was maintained, the form and size were disordered due to the formation of hydroxyl ferric on the surface and in the layer of MMT. Moreover, the inset of Fig. 6 depicted the pore size distribution of the samples calculated from the Barrett-Joyner-Halenda method. The pore size at about 4 nm could be attributed to the "house-of-cards" structure by stacking of the MMT layers, while the pore at size around 25 nm is formed by pillared interlayers [20]. Compared with MMT, the average pore sizes of the Fe-MMT and Fe-MMT-I were decreased, which is in favor of the adsorption and catalytic properties of the materials.

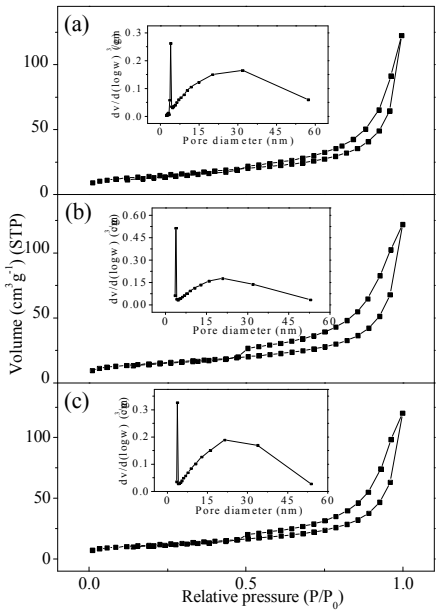

Fig. 6 N_2 adsorption-desorption isotherm and pore size distribution curves (inset) of (a) MMT, (b) Fe-MMT and (c) Fe-MMT-I.

Table 1 Specific surface areas and pore parameters of MMT, Fe-MMT and Fe-MMT-I.

Sample	S_{BET} (m^2/g)	Total pore volume (cm^3/g)	Average pore size (nm)
MMT	50.19	0.1896	15.40
Fe-MMT	49.08	0.1776	12.12
Fe-MMT-I	40.65	0.1858	14.29

3.6 Adsorption performance of Fe-MMT-I

3.6.1 Different adsorbents for the adsorption of RhB Fig. 7 shows the adsorption capacity of RhB on the adsorbents synthesized at different conditions. As we can see from Fig. 7, the adsorption capacity of RhB by the prepared FeOOH and MMT was 6.58 and 80.67 mg/g, respectively. The Fe-MMT synthesized through Fenton process displayed a higher RhB adsorption capacity (112.83 mg/g), which can be ascribed to its high surface area and increased interlayer spacing. It is interesting to observe that the adsorption capacity of RhB by the Fe-MMT-I (148.11 mg/g) was highly increased as compared to that of the Fe-MMT. This results from the fact that the introduction of RhB in the Fenton system leads more hydroxyl ferric inserted into the layer of MMT and further increased the interlayer spacing of MMT. Moreover, it was found that the adsorption capacity of RhB by the Fe-MMT-I I (145.33 mg/g) was comparable to that of the Fe-MMT-I, indicating the general applicability of dyes for the Fenton preparation of Fe-MMT composites with enhanced adsorption activity.

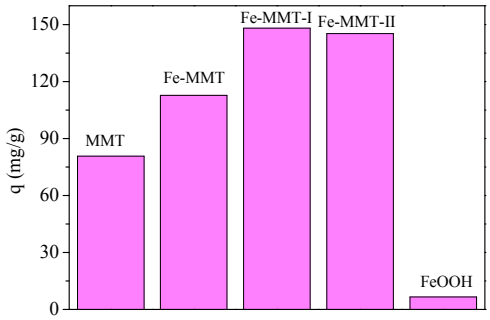

Fig. 7 Effect of different preparation conditions on the adsorption of RhB.

3.6.2 Effect of solution pH on the adsorption of RhB by Fe-MMT-I Solution pH plays a significant role in the adsorption process, thus, the effect of solution pH (2.06-9.72) on the adsorption of RhB by the Fe-MMT-I was determined. As shown in Fig. 8, the adsorption capacity of RhB by the Fe-MMT-I remained constant from pH 2.06 to 4.01 and then decreased. The reason is that when the solution pH is lower than 4, RhB is cationic and monomeric molecular form, which would facilitate the RhB molecular enter into the pore structure of the composite. However, when the solution pH is higher than 4, due to the attractive electrostatic interaction between $-N^+$ and $-COO^-$ groups, the RhB in the solution may aggregate to form bigger molecules and become difficult to enter into the pore of the composite [21].

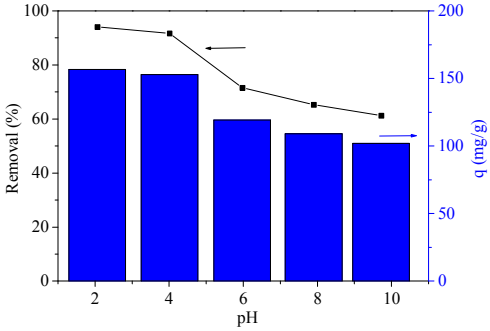

Fig. 8 Effect of initial pH on the adsorption of RhB by Fe-MMT-I.

3.6.3 Kinetic study Fig. 9a depicted the adsorption kinetic curves of RhB by the Fe-MMT-I at different temperatures. It was found that the adsorption capacity of RhB by the Fe-MMT-I was increased dramatically in the first 90 min, and then reached equilibrium gradually at 720 min. The fast adsorption process at the initial stage (0-90 min) indicated that RhB molecules covered on the opened layer surface of the Fe-MMT-I, whereas the slow adsorption rate in later stage could be attributed to the transportation into the interlaminar zone of the adsorbent.

RSC Advances

ARTICLE

Table 2 Kinetic parameters for RhB removal by Fe-MMT-I.

T (°C)	$q_{e,exp}$ (mg/g)	pseudo-first-order model			pseudo-second-order model		
		$q_{e,cal}$ (mg/g)	$k_1\times10^3$ (min^{-1})	R_1^2	$q_{e,cal}$ (mg/g)	$k_2\times10^4$ ((g/mg)/min)	R_2^2
25	152.78	50.90	5.53	0.9114	156.25	3.875	0.9995
35	154.92	53.78	6.45	0.9595	158.73	3.938	0.9996
45	156.56	52.37	7.60	0.9762	158.73	4.731	0.9998

In order to understand the controlling mechanism of the adsorption process, pseudo-first-order and pseudo-second-order equations were applied to fit the adsorption kinetic data. The pseudo-first-order and pseudo-second-order equations are given as [22, 23]:

$$\log(q_e - q_t) = \log q_e - \frac{k_1 t}{2.303} \quad (1)$$

$$\frac{t}{q_t} = \frac{1}{k_2 q_e^{\,2}} + \frac{t}{q_e} \quad (2)$$

where q_e and q_t (mg/g) are the adsorption capacity of RhB at equilibrium and time t (min), respectively, and k_1 (min^{-1}) and k_2 ((g/mg)/min) are the pseudo-first-order and pseudo-second-order rate constants of adsorption, respectively.

The plots of the above models are given in Fig. 9b-c and the calculated kinetic parameters for adsorption of RhB onto the Fe-MMT-I at different temperatures are summarized in Table 2. It is clear that the pseudo-second-order kinetic curves give better fit to the experiment kinetic data with extremely high R^2 (0.9995-0.9998). Besides, the q_e values calculated from the pseudo-second-order kinetic model are closer to the experimental data. All these results suggest chemical sorption as the rate-limiting step of the adsorption mechanism and no involvement of a mass transfer in solution [21].

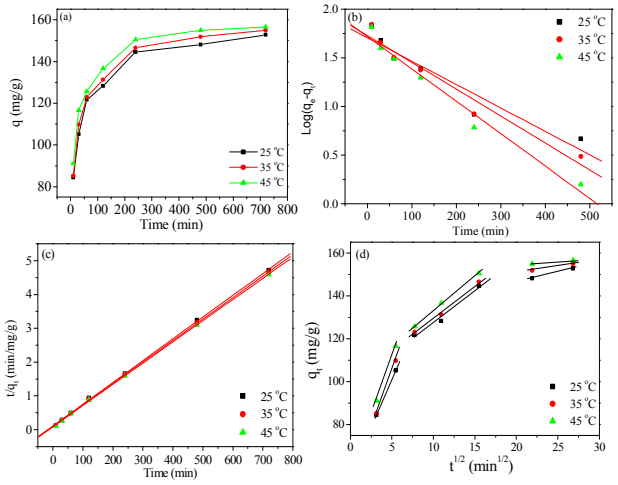

Fig. 9 (a) Effect of contact time for RhB removal by Fe-MMT-I; Fitting curves of (b) pseudo-first-order, (c) pseudo-second-order and (d) intra-particle diffusion equations.

To gain insight into the adsorption mechanism, the experimental data was further subjected to the intra-particle diffusion model, formulated as [24]:

$$q_t = k_3 t^{0.5} + C \quad (3)$$

where k_3 (g/mg/$min^{-0.5}$) is the intra-particle diffusion rate constants and C (mg/g) is the intercept which reflects the boundary layer effect.

Fig. 9d shows the plots of intra-particle diffusion model for the adsorption of RhB onto the Fe-MMT-I at different temperatures. The plots obtained for each temperature can be divided into a muti-linearity correlation, indicating that three stages occurred during the adsorption process: (1) the first stage may be assigned to RhB transportation to the external surface through film diffusion; (2) the second step is a gradual adsorption stage which could be ascribed to intra-particle diffusion; (3) the final stage is due to the low RhB concentration in solution [25, 26]. The above analysis demonstrated that both film diffusion and intra-particle diffusion were simultaneously operating during the adsorption process.

3.6.4 Isotherm Study The equilibrium adsorption isotherms are one of the most important data to describe the adsorption system and to understand the adsorption mechanism. Therefore, the adsorption data were studied by Langmuir, Freundlich and Dubinin–Radushkevich (D–R) adsorption isotherm models with various initial concentrations of RhB at different temperatures. The linear equations are expressed as follows [27-29]:

$$\frac{C_e}{q_e} = \frac{1}{q_m K_L} + \frac{C_e}{q_m} \quad (4)$$

$$\log q_e = \log K_F + \frac{1}{n}\log Ce \quad (5)$$

$$Inq = Inq_m - \beta\varepsilon^2 \quad (6)$$

where q_e is the equilibrium RhB concentration on the adsorbent (mg/g), Ce is the equilibrium concentration (mg/L), q_m and K_L are the Langmuir constants related to the maximum adsorption capacity (mg/g) and adsorption energy (L/mg), respectively, K_F and n are the Freundlich constants depicting the adsorption capacity (L/g) and adsorption intensity, respectively.

RSC Advances

ARTICLE

Table 3 Isotherm parameters for RhB removal by Fe-MMT-I.

T (°C)	Langmuir			Freundlich			Dubinin-Radushkevich (D-R)		
	K_L (L/mg)	R_L range	R^2_L	n	K_F (L/g)	R^2_F	B (mol^2/kJ^2)	R^2_{D-R}	E (kJ/mol)
25	0.53	0.0116-0.0361	0.9998	9.88	137.47	0.9157	0.0008	0.9400	25.00
35	0.64	0.0097-0.0305	0.9999	10.49	143.35	0.9082	0.0007	0.9350	26.73
45	0.73	0.0085-0.0267	0.9999	11.26	150.18	0.8817	0.0006	0.9130	28.87

The plots of Langmuir and Freundlich for the adsorption of RhB onto the Fe-MMT-I at different temperatures are presented in Fig. 10. The parameters and correlation coefficients obtained from these plots are listed in Table 3. Apparently, Langmuir model gives closer fittings than the Freundlich model and the theoretical adsorption capacities are close to the experimental data. All these results suggest the mono-layer chemisorption of RhB onto the Fe-MMT-I [30].

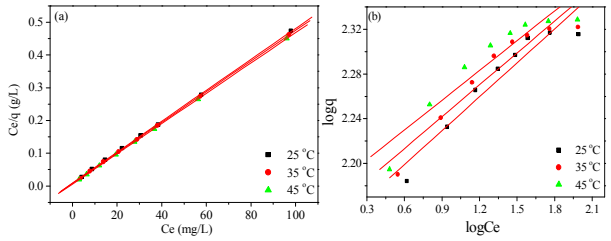

Fig. 10 Fitting curves of (a) Langmuir model and (b) Freundlich model for the adsorption of RhB by Fe-MMT-I.

In addition, the mean energy E could be obtained from the β value calculated from the D-R equation using the following relation [31]:

$$E = \frac{1}{\sqrt{2\beta}} \quad (7)$$

The value of E gives information about the type of adsorption mechanism as chemical or physical adsorption. The magnitude of E value in the range of 1-8 kJ/mol represents a physical nature process while E value higher than 8 kJ/mol corresponds to a chemical process [32]. As can be seen from Table 3, the value of E changes from 25.00-28.87 kJ/mol at all studied temperatures, indicating the adsorption of RhB onto the Fe-MMT-I is chemisorption.

A comparison of the maximum adsorption capacity of RhB onto several well known and common used adsorbents is given in Table 4. The adsorption capacity of the Fe-MMT-I toward RhB is higher than most of the adsorbents reported in the literature, indicating that the Fe-MMT-I composite is a promising adsorbent for the treatment of dye wastewater.

Table 4 Comparison of maximum adsorption capacities with various adsorbents for RhB removal.

Adsorbent	Langmuir capacity (mg/g)	Reference
Kaolinite	46.10	[33]
Na-Montmorillonite	38.27	[34]
Anaerobic sludge	19.52	[35]
Fe-supported bentonite	227.27	[36]
Fe-pillared bentonite	98.62	[37]
Fly ash	10.00	[38]
RGO-ZnO	32.60	[39]
Modified Fe_3O_4	161.80	[40]
Acid-Montmorillonite	185.18	[41]
Fe-MMT-I	207.50	This work

3.6.5 Regeneration and recycle In order to reduce the cost of the adsorption process and minimize the potential problem of secondary pollution, the spent adsorbent should be regenerated and used from the perspective of both economic and environmental protection. Previous literatures have reported many regeneration methods such as washing with acid or alkali solution, calcining at a high temperature and reducing in partial pressure [42-44]. However, these methods have some disadvantages such as requiring a high cost or time-consuming. In the present work, a new heterogeneous photo-Fenton regeneration method was utilized. According to the Haber-Weiss mechanism, the removal of RhB can be described by equations 8-10, which include the adsorption and decomposition of H_2O_2, the reduction of Fe^{3+} and the generation of the hydroxyl radicals (•OH) through heterogeneous Fenton process [45-47].

$$Fe^{3+} + vis \rightarrow Fe^{2+} \quad (8)$$

$$Fe^{2+} + H_2O_2 \rightarrow Fe^{2+} \bullet H_2O_2 \rightarrow Fe^{3+} + \bullet OH + OH^- \quad (9)$$

$$Fe^{3+} + H_2O_2 \rightarrow Fe^{3+} \bullet H_2O_2 \rightarrow Fe^{2+} + \bullet OOH + H^+ \quad (10)$$

Fig. 11 demonstrates the heterogeneous photo-Fenton regeneration of RhB by the Fe-MMT-I as a function of regeneration times. After five recycles, the Fe-MMT-I did not exhibit significant loss of the adsorption capacity toward RhB, indicating that the adsorbent has a great potential application value.

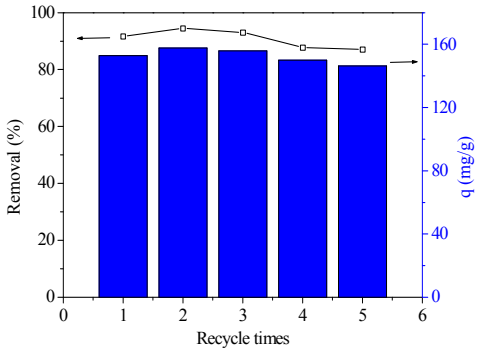

Fig. 11 Effect of regeneration times on the discoloration of RhB by Fe-MMT-I.

3.7 Heterogeneous Fenton performance of Fe-MMT-I

3.7.1 Catalytic activity Fig. 12 displays the degradation of RhB under different conditions. As shown in Fig. 12a, under vis irradiation, little discoloration of RhB was achieved in the presence of H_2O_2. The discoloration of RhB was increased significantly with the Fe-MMT-I, which could be ascribed to the high adsorption capacity of the Fe-MMT-I toward RhB. However, under the cooperative effect of H_2O_2 and vis irradiation, the discoloration of RhB by the Fe-MMT-I reached more than 99% within 60 min. Under the same condition, the Fe-MMT also showed high discoloration efficiency toward RhB, however, due to the lower adsorption capacity toward RhB, the discoloration rate of the Fe-MMT is not as fast as that of the Fe-MMT-I.

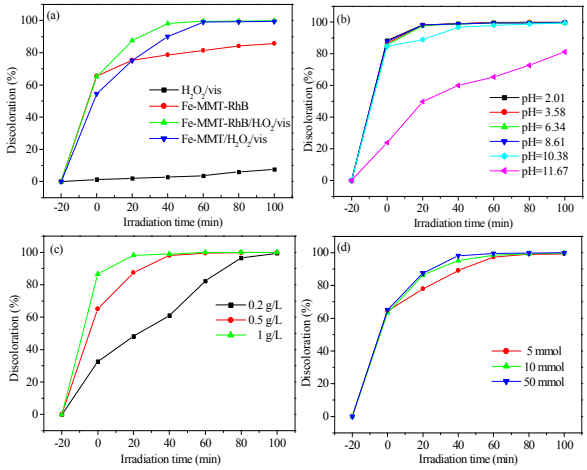

Fig. 12 Photo-Fenton discoloration of RhB: (a) under different conditions; (b) effect of solution pH; (c) effect of Fe-MMT-I dosage; (d) effect of H_2O_2 dosage.

The effects of solution pH, catalyst dosage and H_2O_2 dosage on the discoloration of RhB by the Fe-MMT-I/H_2O_2/vis system are presented in Fig 12b-d. The discoloration of RhB by the Fe-MMT-I was increased with the increase of catalyst and H_2O_2 dosage, however, from the viewpoint of economic cost, the catalyst and H_2O_2 dosage may be optimized as 0.5 g/L and 10 mmol, respectively. As for the effect of solution pH, it is clear seen from Fig. 12b that the Fe-MMT-I catalyst exhibited high discoloration efficiency toward RhB over a wide pH range of 2.01-10.38, the discoloration of RhB by the catalyst was over 80% even when the pH was increased to 11.67. The result indicates that the Fe-MMT-I catalyst could overcome the disadvantage of the narrow pH operating range in homogeneous Fenton system.

3.7.2 Stability of the Fe-MMT-I The reusability and stability of a catalyst are important factors for practical application. The regeneration of the Fe-MMT-I showed its excellent reusability, FT-IR analysis was used to further confirmed the stability of the Fe-MMT-I. As shown in Fig. 13, a few characteristic peaks of RhB are clearly seen in the spectrum of the RhB saturated Fe-MMT-I, such as bands at 1592, 1414, 1339, 1247 and 1181 cm^{-1}, corresponding to the stretching vibration mode of C=C, bending vibration of CH_2, stretching vibration of C-N linked with benzene ring, stretching vibration of C-N in -N(C_2H_5) and asymmetry stretching vibration of C-O-C, respectively [48]. After reaction, the RhB characteristic peaks disappeared completed, suggesting that the RhB on the Fe-MMT-I was degraded. Furthermore, the spectra of the Fe-MMT-I catalyst before and after degradation did not show significant changes, demonstrating the good stability of the catalyst.

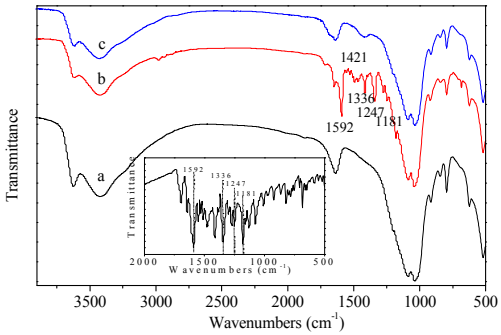

Fig. 13 FT-IR spectra of Fe-MMT-I for different degradation times: (a) fresh Fe-MMT-I; (b) 0 min; (c) 100 min. The inset is FT-IR spectrum of pure RhB.

3.7.3 Mechanism discussion Generally, •OH radicals are known as the main active species in the heterogeneous Fenton process, which can be detected by the terephthalic acid (TA) photoluminescence (PL) probing technique [49]. It is well established that the generation of •OH radicals in the heterogeneous photo-Fenton reaction can be observed by the increased PL intensity at 426 nm due to the formation of strongly luminescing 2-hydroxylterephthalic acid (HTA). Fig. 14a shows the PL spectra of the Fe-MMT-I/H_2O_2/vis/TA system during the degradation process. It is obvious that the PL intensity at 426 nm increases continuously with increased irradiation time and the increasing tendency is consistent with that of the discoloration of RhB (Fig. 12a), indicating that •OH radicals were the main active species for the Fe-MMT-I /H_2O_2/vis system.

To explore whether the •OH radicals generated during the reaction are heterogeneously initiated or homogeneously initiated, the homogeneous photo-Fenton experiment was carried out under the same condition using iron salts (4.18 mg/L Fe^{3+}) based on the amount of iron leaching from the catalyst after the first run. As can be seen from Fig. 14b, the

RhB discoloration by the Fe^{3+}/H_2O_2/vis system was only 38.25% after 100 min, which was far less than that by the Fe-MMT-I /H_2O_2/vis system (99.94%). The result demonstrates that the •OH radicals generated by heterogeneous Fenton process predominated.

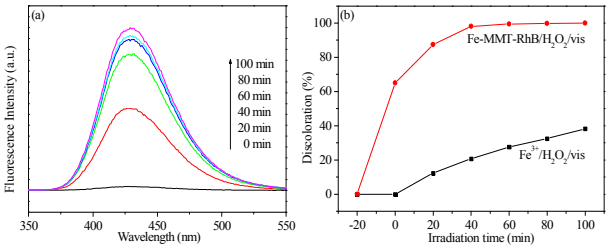

Fig. 14 (a) •OH-trapping photoluminescence spectra of Fe-MMT-I/H_2O_2/vis/TA solution; (b) Discoloration of RhB under Fe^{3+}/H_2O_2/vis and Fe-MMT-I/H_2O_2/vis systems.

4. Conclusions

In summary, the bifunctional Fe-MMT-I composite was fabricated during the Fenton degradation of RhB. XRD and SEM results confirmed the existence of FeOOH both in the layer and on the surface of the composite. The adsorption of RhB onto the Fe-MMT-I can be well described by the pseudo-second-order model and the Langmuir isotherm model, indicating a monolayer adsorption process. The maximum adsorption capacity of the Fe-MMT-I toward RhB is 207.50 mg/g, which is higher than most of the adsorbents reported in the literature. The high adsorption capacity of the composite could be attributed to the increased basal spacing which resulted from the introduction of RhB during the preparation process. The result also showed that the Fe-MMT-I still exhibited high adsorption capacity toward RhB after five recycles using heterogeneous Fenton method to regenerate the spent adsorbent. The Fe-MMT-II also possessed high adsorption capacity of RhB indicating the general applicability of dyes for the Fenton preparation of Fe-MMT composites with enhanced adsorption property. Moreover, under optimal conditions, the Fe-MMT-I composite exhibited excellent discoloration of RhB with good stability and wide operating pH range (2.01-11.67) in the presence of H_2O_2, which could be ascribed to the synergetic effects of the enhanced adsorption powder of the composite and the •OH radicals initiated through heterogeneous Fenton process. The present work may provide new insight into designing and fabricating novel bifunctional composites for environmental remediation.

Acknowledgements

This work was supported by National Key Technology R&D Program of China (2012BAJ25B02-03), Program of Specialized Research Fund for the Doctoral Program of Higher Education (20110143110015) and the fundamental Research Funds for the Central Universities (2014-yb-005).

References

1. J. T. Zhang, W. S. Zhu, H. M. Li, Y. Q. Jiang, W. L. Huang and Y. S. Yan, *Green Chem.*, 2009, **11**, 1801-1807.
2. W. S. Zhu, J. T. Zhang, H. M. Li, Y. H. Chao, W. Jiang, S. Yin and H. Liu, *RSC Adv.*, 2012, **2**, 658-664.
3. S. Guo, G. K. Zhang, Y. D. Guo and J. C. Yu, *Carbon*, 2013, **60**, 437-444.
4. L. J. Xu and J. L. Wang, *Appl. Catal. B: Environ.*, 2012, **123**, 117-126.
5. J. H. Deng, J. Y. Jiang, Y. Y. Zhang, X. P. Lin, C. M. Du and Y. Xiong, *Appl. Catal. B: Environ.*, 2008, **84**, 468-473.
6. Z. P. Wen, Y. L. Zhang, C. M. Dai and Z. Sun, *J. Hazard. Mater.*, 2015, **287**, 225-233.
7. J. Liu and G. K. Zhang, *Phys. Chem. Chem. Phys.*, 2014, **16**, 8178-8192.
8. A. Ausavasukhi and T. Sooknoi, *Green Chem.*, 2015, **17**, 435-441.
9. T. Polubesova, S. Eldad and B. Chefetz, *Environ. Sci. Technol.*, 2010, **44**, 4203-4209.
10. X. J. Peng, Z. K. Luan and H. M. Zhang, *Chemosphere*, 2006, **63**, 300-306.
11. N. K. Daud, M. A. Ahmad and B. H. Hameed, *Chem. Eng. J.*, 2010, **165**, 111-116.
12. H. Tamura, K. Goto, T. Yotsuyanagi and M. Nagayama, *Talanta*, 1974, **21**, 314-318.
13. C. Chen, D. W. Park and W. S. Ahn, *Appl. Clay Sci.*, 2013, **283**, 699-704.
14. L. Liu, L. Q. Yang, H. W. Liang, H. P. Cong, J. Jiang and S. H. Yu, *ACS Nano*, 2013, **7**, 1368-1378.
15. M. Baek, J. H. Choy and S. J. Choi, *Int. J. Pharmaceut.*, 2012, **425**, 29-34.
16. H. A. Patel, R. S. Somani, H. C. Bajaj and R. V. Jasra, *Appl. Clay Sci.*, 2007, **35**, 194-200.
17. B. Iurascu , I. Siminiceanu , D. Vione, M. A. Vicente and A. Gil, *Water Res.*, 2009, **43**, 1313-1322.
18. C. Luengo, V. Puccia and M. Avena, *J. Hazard. Mater.*, 2011, **186**, 1713-1719.
19. B. S. Li, Z. X. Liu, C. Y. Han, W. Ma and S. J. Zhao, *J. Colloid Interface Sci.*, 2012, **377**, 334-341.
20. Y. Li, J. R. Liu, S. Y. Jia, J. W. Guo, J. Zhuo and P. Na, *Chem. Eng. J.*, 2012, **191**, 66-74.
21. J. Anandkumar and B. Mandal, *J. Hazard. Mater.*, 2011, **186**, 1088-1096.
22. S. Largergren, *Kungliga Svenska Vetenskapsakademiens, Handlingar* 1898, **24**, 1-39.
23. Y. S. Ho and G. McKay, *Process. Biochem.*, 1999, **34**, 451-465.
24. W. J. Weber and J. C. Morris, *J. Sanit. Eng. Div. Am. Soc. Civ. Eng.* 1963, **89**, 31-60.
25. H. Chen, Y. G. Zhao and A. Q. Wang, *J. Hazard. Mater.*, 2007, **149**, 346-354.
26. Y. Li, Q. Y. Yue and B. Y. Gao, *J. Hazard. Mater.*, 2010, **178**, 455-461.
27. Langmuir, *J. Am. Chem. Soc.*, 1918, **40**, 1361-1403.
28. H. Freundlich, *Z. Phys. Chem.*, 1906, **57**, 385–470.
29. M. M. Dubinin, E. D. Zaverina and L. V. Radushkevich, *Zh. Fiz. Khim.*, 1947, **21**, 1351–1362.
30. G. Zhang, I. Y. Song, T. Park and W. Y. Choi, *Green Chem.*, 2012, **14**, 618-621.
31. P. Hobson, *J. Phys. Chem.*, 1969, **73**, 2720-2727.
32. X. Mi, G. B. Huang, W. S. Xie, Y. Liu and J. P. Gao, *Carbon*, 2012, **50**, 4856-4864.
33. T. A. Khan, S. Dahiya and I. Ali, *Appl. Clay Sci.*, 2012, **69**, 58-66.
34. P. P. Selvam, S. Preethi, P. Basakaralingam, N. Thinakaran, A. Sivasamy and S. Sivanesan, *J. Hazard. Mater.*, 2008, **155**, 39-44.
35. Y. Wang, Y. Mu, Q. B. Zhao and H. Q. Yu, *Sep. Purif. Technol.*, 2006, **50**, 1-7.

36. Y. W. Gao, Y. Wang and H. Zhang, *Appl. Catal. B: Environ.*, 2014, **178**, 29-36.
37. M. F. Hou, C. X. Ma, W. D. Zhang, X. Y. Tang, Y. N. Fan and H. F. Wan, *J. Hazard. Mater.*, 2011, **186**, 1118-1123.
38. S. H. Chang, K. S. Wang, H. C. Li, M. Y. Wey and J. D. Chou, *J. Hazard. Mater.*, 2009, **172**, 1131-1136.
39. F. Wang, T. Tsuzuki, B. Tang, X. L. Hou, L. Sun and X. G. Wang, *ACS Appl. Mater. Inter.*, 2012, **4**, 3084-3090.
40. Peng, P. F. Qin, M. Lei, Q. R. Zeng, H. J. Song, J. Yang, J. H. Shao, B. H. Liao and J. D. Gu, *J. Hazard. Mater.*, 2012, **209**, 193-198.
41. K. G. Bhattacharyya, S. SenGupta and G. K. Sarma, *Appl. Clay Sci.*, 2014, **99**, 7-17.
42. Y. L. Qin, M. C. Long, B. H. Tan and B. X. Zhou, *Nano-Micro Lett.*, 2014, **6**, 125-135.
43. D. Mugisidi, A. Ranaldo, J. W. Soedarsono and M. Hikam, *Carbon*, 2007, **45**, 1081-1084.
44. Y. Zhou, J. Fan, G. K. Cui, X. M. Shang, Q. H. Tang, J. J. Wang and M. H. Fan, *Green Chem.*, 2014, **16**, 4009-4016.
45. S. Guo, G. K. Zhang and J. Q. Wang, *J. Colloid Interface Sci.*, 2014, **433**, 1-8.
46. S. Guo, G. K. Zhang and J. C. Yu. *J. Colloid Interface Sci.*, 2015, **448**, 460-466.
47. W. Luo, L. H. Zhu, N. Wang, H. Q. Tang, M. J. Cao and Y. B. She, *Environ. Sci. Technol.*, 2010, **44**, 1786-1791.
48. G. K. Zhang, Y. Y. Gao, Y. L. Zhang and Y. D. Guo, *Environ. Sci. Technol.*, 2010, **44**, 6384-6389.
49. S. Y. Wang, B. B. Huang, Z. Y. Wang, Y. Y. Liu, W. Wei, X. Y. Qin, X. Y. Zhang and Y. Dai, *Dalton Trans.*, 2011, 40, 12670-12675.

Graphical Abstract